Physica B 521 (2017) 141–147

Contents lists available at ScienceDirect

Physica B

journal homepage: www.elsevier.com/locate/physb

Surface functionalization of magnetite nanoparticle: A new approach using condensation of alkoxysilanes

A.F.R. Rodriguez[a,*], T.P. Costa[b], R.A. Bini[b], F.S.E.D.V. Faria[a], R.B. Azevedo[c], M. Jafelicci Jr, [b], J.A.H. Coaquira[d], M.A.R. Martínez[d], J.C. Mantilla[d], R.F.C. Marques[b], P.C. Morais[d,e]

[a] Postgraduate Studies in Biotechnology and Biodiversity, Federal University of Acre, Rio Branco, Acre, Brazil
[b] Department of Physical Chemistry, Institute of Chemistry, Universidade Estadual Paulista, Araraquara, São Paulo, Brazil
[c] Universidade de Brasília, Instituto de Ciências Biológicas, Brasília DF 70910-900, Brazil
[d] Universidade de Brasília, Instituto de Física, Brasília DF 70910-900, Brazil
[e] Anhui University, School of Chemistry and Chemical Engineering, Hefei 230601, China

ARTICLE INFO

Keywords:
Magnetite nanoparticles
Surface-functionalization
Hydrolysis and condensation reactions
X-ray diffraction
Mössbauer spectroscopy
Zero-field-cooled/field-cooled traces

ABSTRACT

In this study we report on successful production of two samples (BR15 and BR16) comprising magnetite (Fe_3O_4) nanoparticles (~10 nm) surface-functionalized via hydrolysis and condensation of alkoxysilane agents, namely 3-aminopropyl-trimethoxisilane (APTS) and N-propyl-trimethoxisilane (NPTS). The as-produced samples were characterized using transmission electron microscopy (TEM), x-ray diffraction (XRD), magnetization measurements (5 K and 300 K hysteresis cycles and zero field-cooled/field-cooled measurements), and Mössbauer spectroscopy (77 and 297 K). The Mössbauer data supported the model picture of a core-shell magnetite-based system. This material system shows shell properties influenced by the surface-coating design, either APTS-coated (BR15) or APTS+NPTS-coated (sample BR16). Analyses of the Mössbauer spectra indicates that the APTS-coated sample presents Fe(III)-rich core and Fe(II)-rich shell with strong hyperfine field; whereas, the APTS+NPTS-coated sample leads to a mixture of two main nanostructures, one essentially surface-terminated with APTS whereas the other surface-terminated with NPTS, both presenting weak hyperfine fields compared with the single surface-coated sample. Magnetization measurements support the core-shell picture built from the analyses of the Mössbauer data. Our findings emphasize the capability of the Mössbauer spectroscopy in assessing subtle differences in surface-functionalized iron-based core-shell nanostructures.

1. Introduction

Nowadays magnetic nanoparticles (MNPs) are essential building blocks in nanotechnology, supporting a wide variety of industrial and biomedical applications [1]. As far as the biomedical applications are concerned superparamagnetism is unique while allowing remote manipulation (under gradient of magnetic field) and heating (under alternate magnetic field) of nanomaterials [2]. Besides, magnetic nanomaterials, such as magnetic nanoparticles and molecular magnets, are very much interesting from the basic point of view [3]. Surface functionalization of magnetic iron oxide nanoparticles using bioactive moieties supports different technologies, such as magnetic drug delivering, magnetohyperthermia and contrast agent for magnetic resonance imaging [4,5]. In recent years, surface functionalization of metal-oxide magnetic nanoparticles has been receiving much attention with major impact while developing new nanobiocompatible products [6–8]. For human imaging purpose, superparamagnetic iron oxide (SPIO) particles need to be biocompatible while providing a safe route of elimination [9]. Also, SPIO particles, like cubic ferrites, can be surface functionalized and therefore tailored to bind to a wide variety of drugs, proteins, enzymes, antibodies, and cell targets [10].

On the other hand, SPIO particles show very interesting basic phenomena such as quantum confinement of carriers and magnetic quantum tunneling effect [11,12]. These phenomena are connected with quantum size effect and superparamagnetic behavior, which support surface charge modulation from negative to positive (thus allowing surface functionalization with different moieties) and external manipulation (magnetic pliers) using gradients of magnetic field. Besides, single nanoparticles core-shell structures, with a reactive molecular shell (RMS) around the metal-oxide core, provide extra opportunity for surface functionalization of the core magnetic nanoparticle [13]. In searching for RMS candidates, we have finding those that can offer reactive amino groups facing outside the shell, which may provide important breakthroughs as far as the biological and medical

* Corresponding author.
E-mail addresses: ruiz@ufac.br, anselmorodriguez73@gmail.com (A.F.R. Rodriguez).

http://dx.doi.org/10.1016/j.physb.2017.06.043
Received 10 March 2017; Received in revised form 30 May 2017; Accepted 15 June 2017
Available online 16 June 2017

applications are concerned. In this regard hydrolysis and condensation of alkoxysilane agents onto metal-oxide surfaces represent an excellent approach.

Hence, comprehensive characterization of the magnetic behavior of the end nanostructure is of major interest. This can be addressed by several and well-established experimental techniques, such as the superconducting quantum interference device magnetometry and Mössbauer spectroscopy. In this study, we reported on the successful preparation and magnetic characterization of surface amino-modulated nanosized magnetite particles. Discussion of the Mössbauer data revealed new insights regarding the effect of surface coating species in the iron oxide-based core's properties and will be supported by transmission electron microscopy (TEM) data, x-ray diffraction (XRD) patterns, and magnetometry.

2. Experimental section

Iron (II) and iron (III) chlorides (Aldrich 98%), 3-aminopropyl-triethoxisilane (Aldrich 97%), N-propyl-triethoxisilane (Aldrich 97%) and ethanol absolute (Panreac) were used as received. Distilled water was used throughout all preparation procedures. Surface functionalized magnetite nanoparticles were preparing using a two-step protocol, as shortly described herein. Firstly, nanosized magnetite (Fe_3O_4) had been synthesizing by a new sonoprecipitation method developed by Marques et al. [14]. Secondly, surface functionalized magnetite-based samples, labeled BR15 and BR16, had been preparing via hydrolysis and condensation of two organosilane agents, namely 3-aminopropyl-triethoxisilane (APTS) and N-propyl-triethoxisilane (NPTS), schematically represented in Fig. 1. The as-synthesized magnetite nanoparticle was silylating using the silane-based coupling agents in aqueous-alcohol solution. Two aqueous-alcohol solutions containing the silane-based agents were preparing by adding 0.3 mL of APTS (for sample BR15) or 0.15 mL of APTS plus 0.15 mL of NPTS (for sample BR16) into 10 mL of 95% ethanol-5% water solution. The native magnetite nanoparticle were adding to the APTS or APTS and NPTS solutions and the resultant solution was refluxing at 85 °C for 2 h. The as-produced samples (BR15 and BR16) were washing several times with ethanol.

➡ For the absolute determination of the amine density on the nanoparticles surface of samples prepared in this work the methodology proposed by Moon J.H. et al. [15–17] was used. The methodology consists of the reaction between an aldehyde and amine groups on the surface of NP forming imines. Imines are unstable in aqueous medium and are readily hydrolyzed to form the aldehyde and the amine again. Thus, the colorimetric determination of the aldehydes released after the hydrolysis of the imines allows the indirect determination of the concentration of amines on the surface of the NPs.

The shape and size of the surface functionalized magnetite nanoparticles were examining by a Philips CM 120 transmission electron microscope (TEM) operating at 120 kV. Briefly, dried samples of the as-produced nanoparticles were dispersing in isopropyl alcohol and cast onto amorphous carbon-coated copper grids for imaging. The crystalline structure of the samples was investigating by x-ray diffraction (XRD) using a Philips powder diffractometer PW 3040/60 operating with Cu-Kα radiation. X-ray fluorescence spectroscopy measurements had been carrying out using a Shimadzu spectrometer EDX-72. The relative amount of Fe and Si were determining to be respectively 97% and 3% (sample BR16) and 80% and 20% (sample BR15). ^{57}Fe Mössbauer spectra were recording at 77 and 297 K using a conventional constant acceleration transmission spectrometer with a ^{57}Co(Rh) source and a bath cryostat. The recorded spectra had been fitting using the MOSSWIN program whereas α-Fe foil had been using for calibration. Values of the isomer shift (*IS*) had quoted with respect to α-Fe at room temperature. DC magnetic measurements were carrying out using a MPMS3 (Quantum Design, Inc) Superconducting Quantum Interference Device (SQUID) magnetometer. Applied magnetic field varied from 0 up to ± 70 kOe whereas the sample temperature scanned in the temperature range from 5 to 300 K.

3. Results and discussion

Typical TEM micrographs (see Fig. 2) of sample BR15 (BR16) revealed spherically shaped magnetite nanoparticle. Those images had been using to count 340 and 210 nanoparticles for samples BR15 and BR16, respectively, in order to mount the histograms showed in Fig. 2. The histograms have been modeling using the lognormal distribution function [18]. The fit of data provides the average diameter (D_{TEM}) of 9.9 (10.5) nm for sample BR15 (BR16) and diameter dispersion (σ_{TEM}) of 0.23 (0.22) for sample BR15 (BR16). The XRD data (see Fig. 3) of samples BR15 and BR16 presented broad x-ray diffraction peaks, characteristic of nanoparticulated materials. The Bragg peak positions identified in both samples (BR15 and BR16) are in accordance with the standard values of the magnetite phase (JCPDS card No. 19–0629). The (3 1 1) XRD peak (see Fig. 3) of both samples (BR15 and BR16) have been using to estimate the crystallite size (D_{XRD}) employing the Scherrer's approximation (see data in Table 1). Diameter values estimated from the XRD data (D_{XRD}) are in good agreement with those obtained from the TEM image analyses (D_{TEM}). The larger values find for D_{TEM} (9.9 and 10.5 nm) while compared to D_{XRD} (7.9 nm) is likely due to the lack of good crystallinity at the surface layer, as already reported in the literature [19]. Table 1 also collected the values we find for the lattice parameter (a) and the (3 1 1) interplanar spacing (d_{311}) of samples BR15 and BR16, which are in good agreement with the standard values reported for magnetite.

➡ The amino group density for samples BR15 and BR16 was 18.47 mMol/mg and 31.5 mMol/mg of sample, respectively. The inversely proportional dependence of the amine groups density on

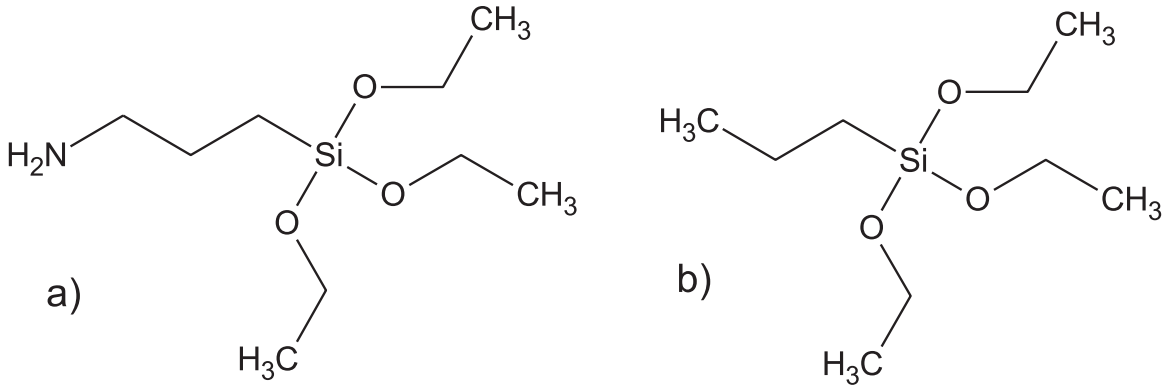

Fig. 1. (a) Chemical structure of APTS alkoxysilane and (b) Chemical structure of NPTS alkoxysilane.

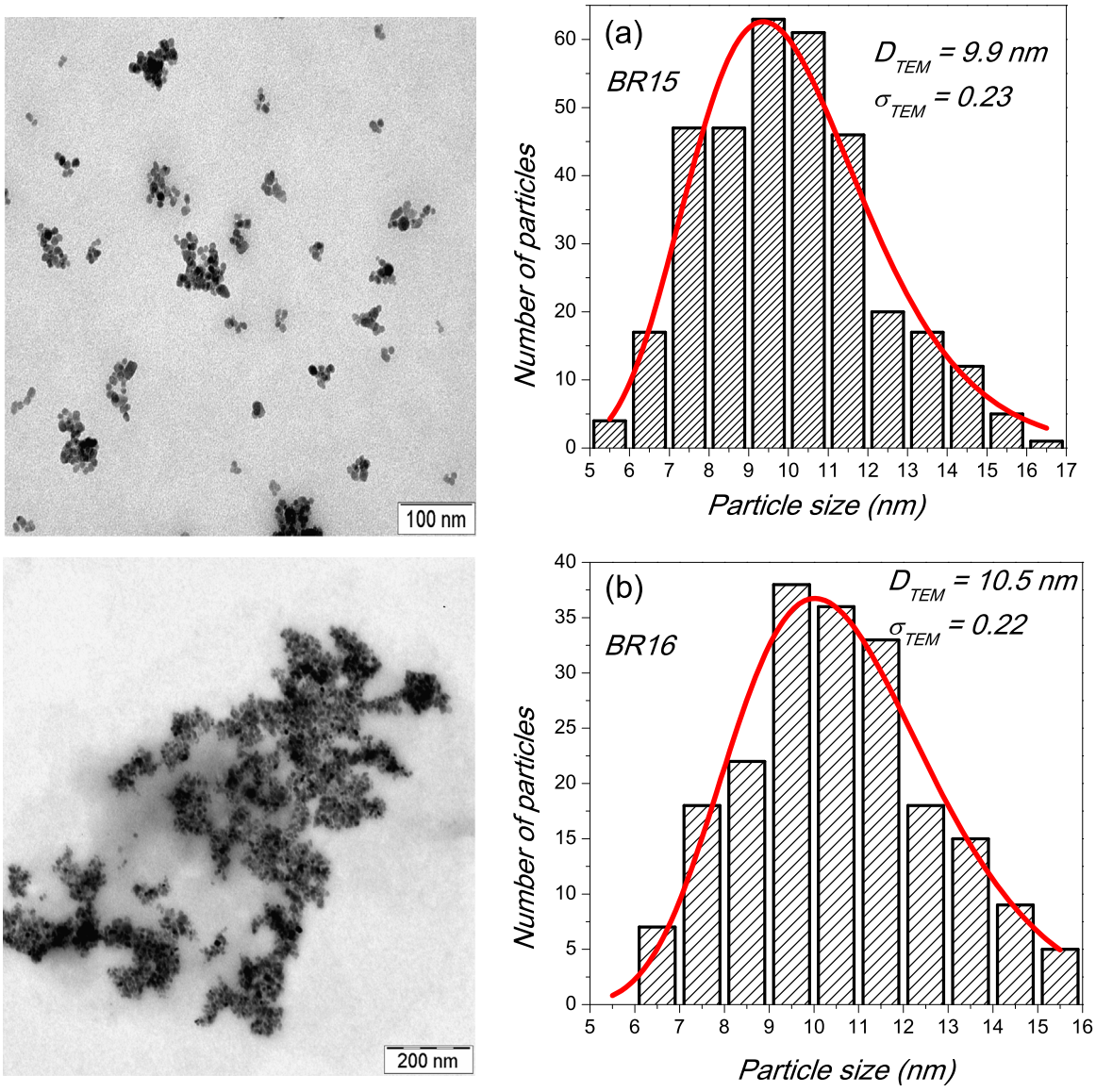

Fig. 2. TEM micrographs and corresponding particle size histograms of samples (a) BR15 and (b) BR16.

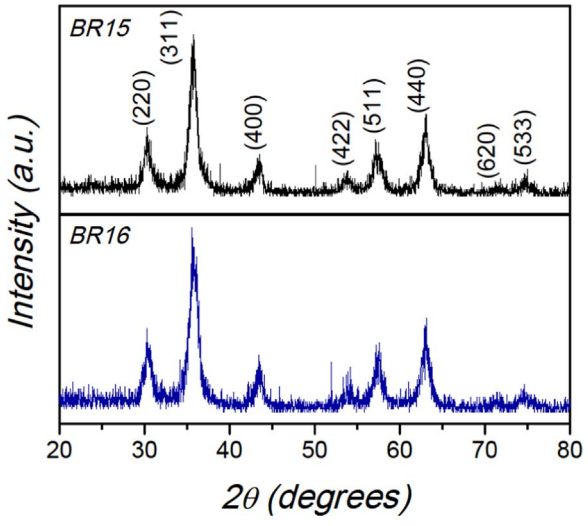

Fig. 3. X-ray diffraction patterns of samples BR15 and BR16.

Table 1
Lattice parameter (a), distance between 311 planes (d_{311}), and crystallite diameter (D_{XRD}).

Sample	a (Å)	d_{311} (Å)	D_{XRD} (nm)
BR15	8.34	2.51	7.9
BR16	8.35	2.52	7.9

the samples surface functionalized with APTS-NPTS can be explained in terms of the hydrolysis rate difference of the APTS and NPTS. In addition to the hydrolysis rate of the alkoxysilanes, the oscillatory mechanism of APTS adsorption on iron oxide surfaces must be considered. In 1990, H. Linde [20] suggested a dynamic model for the interaction of APTS with silica surfaces. The author postulated that the terminal amine group of the APTS molecule initially formed a salt with the hydroxyl groups on the surface and subsequently this orientation is reversed and the silane groups at the other end of the molecule will bound to the surface via siloxane bonds. In 1996, I. George et al. [21], demonstrated this mechanism through XPS (X-ray

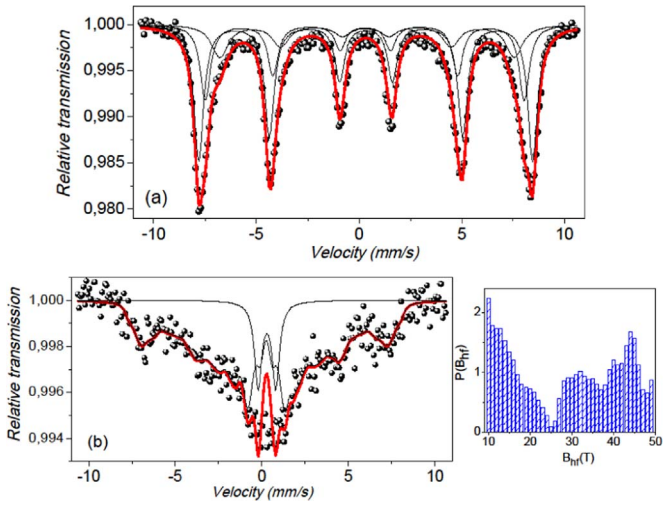

Fig. 4. (a) 77 K Mössbauer spectra of sample BR15 and (b) Room-temperature Mössbauer spectra of sample BR15 with the corresponding distribution of hyperfine field on the right hand-side.

photoelectron spectroscopy) analysis of the interface of APTS / silica films exposed to the ambient atmosphere and at different temperatures. On the other hand, studies of the adsorption of NPTS on iron oxide surfaces indicated that, unlike the APTS result, the oscillatory mechanism is not observed [22]. In contrast, the adsorption profile of NPTS in iron oxide exhibited behavior related to the Langmuir adsorption isotherm [23], indicating that the NPTS is adsorbed individually on the surface of the iron oxide until all the sites are occupied, saturating the surface. Thus, based on the observations and results of other similar systems investigated and reported in the literature, the mechanism of hydrolysis of the APTS-NPTS mixture can be inferred through a competitive adsorption model between APTS and NPTS before condensation. The hypothesis for increasing the amine density on the surface of the NP should consider the larger surface area of the NP functionalized with the APTS-NPTS mixture, due to the presence of a layer of NPTS covering the NP before the APTS condense on it.

Low-temperature (77 K) Mössbauer spectra of samples BR15 and BR16 (see upper panel in Figs. 4 and 5) are well resolved using three sextets (black solid lines); two of them describing iron ions in tetrahedral (A) and octahedral (B) sites in the core magnetite nanoparticle. The third component however, showing the weakest hyperfine field (B_{hf}) and the broadest linewidth (Γ), has been assigning to iron ions located in defective sites, likely at the nanoparticle surface of the magnetite core where the density of defects (such as vacancies) is enhanced and the iron ions present a reduced coordination number due to the lack of translational symmetry. At room temperature (297 K), the Mössbauer spectra of samples BR15 and BR16 (see lower panel in Figs. 4 and 5) were curve-fitted using a doublet and a distribution of sextets, which represents a distribution of hyperfine fields and indicates the occurrence of magnetic collapse due to thermal relaxation of the particle's magnetic moment. The distributions of hyperfine fields obtained from the fittings of the room temperature Mössbauer spectra (samples BR15 and BR16) were also showed in Figs. 4 and 5. The room temperature Mössbauer doublet, with different values of isomer shift (*IS*) and quadrupole splitting (*QS*) for samples BR15 and BR16, represents the already relaxed particles and is included in the central part of the spectra [24]. Mössbauer parameters obtained from the fittings were collecting in Table 2.

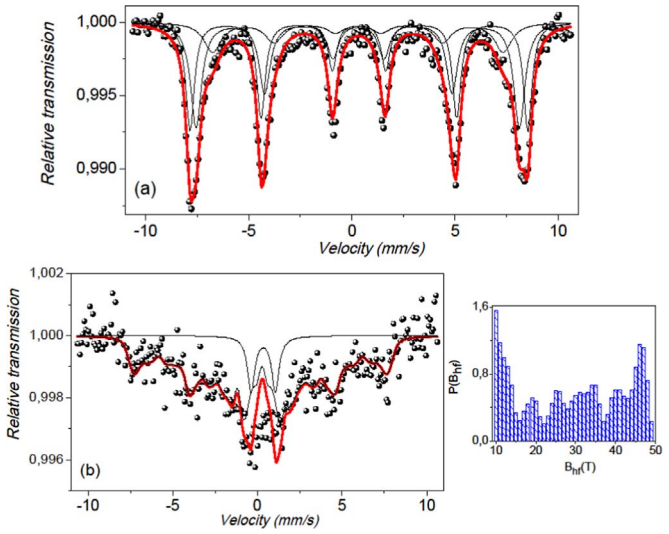

Fig. 5. (a) 77 K Mössbauer spectra of sample BR16 and (b) Room-temperature Mössbauer spectra of sample BR16 with the corresponding distribution of hyperfine field on the right hand-side.

➡ Differences observed in the Mössbauer data (see Table 2), particularly in regard to the weakest hyperfine field component at 77 K (B_{hf} and *IS* values), which has been ascribing to the shell magnetite nanoparticle, indicate major differences in the surface coating of both samples (BR15 and BR16). Additionally, the hyperfine field distributions obtained from the room temperature Mössbauer spectra (see Figs. 4 and 5) are quite different and may reflect the samples' surface coating differences as well. Note that the low temperature (77 K) Mössbauer parameters associated to the core magnetite nanoparticle (the two strongest hyperfine field components) show negligible differences for both samples. Therefore, the explanation for the differences observed in the room temperature Mössbauer spectra is associated to the shell magnetite nanoparticle and it is more likely correlated with the use of just one surface coating species to produce sample BR15 as opposed to two surface coating species while producing sample BR16. Moreover, sample BR15 is supposed to present one main nanostructure (Fe_3O_4@ATPS) whereas sample BR16 may present two main nanostructures (Fe_3O_4@ATPS/NPTS and Fe_3O_4@NPTS/ATPS), which are different because they are either dominantly terminated with NPTS or ATPS. In the BR15 sample the free electron pair of the ATPS's amino group likely coordinates to iron ions at the nanoparticle surface, polarizing the shell magnetite nanoparticle and shifting the surface's character towards Fe(II)-rich, thus revealing a higher isomer shift of 0.47 mm/s and 0.39 mm/s associated to the Mössbauer sextets at 77 K and 297 K, respectively. Meanwhile, in the BR15 sample, the core magnetite nanoparticle may transfer electrons outwards to the shell magnetite nanoparticle, shifting the core's character towards Fe(III)-rich, thus presenting a lower isomer shift of 0.41 mm/s at 297 K. On the other hand, in the BR16 sample, the possibility of a double molecular coating layer (ATPS plus NPTS) may produce a final sample composed of two main nanostructures, as mentioned above (Fe_3O_4@ATPS/NPTS and Fe_3O_4@NPTS/ATPS). It is reasonable to expect differences in *IS* values associated to the Mössbauer sextets while examining the two nanostructures Fe_3O_4@ATPS(inner-shell)/NPTS(outer-shell) and Fe_3O_4@NPTS(inner-shell)/ATPS(outer-shell). However, the effective *IS* values associated to the Mössbauer sextets of the end sample may change slightly, depending upon the relative fraction of the two possible nanostructures, as observed in the data presented in Table 2. Then, the reduction of the *IS* (0.41 mm/s and 0.37 mm/s) of sample BR16 (77 K and 297 K) with respect to the *IS* (0.47 mm/s and 0.39 mm/s) of sample BR15 (77 K and 297 K) more likely reflect the influence of the Fe_3O_4@NPTS(inner-shell)/ATPS(outer-shell) nanostructure. The lower room temperature *QS* value associated to the doublet of sample BR15 (1.02 mm/s) with respect to sample BR16 (1.43 mm/s) supports the model picture of a Fe(III)-richer core magnetite nanoparticle for the sample BR15. Additionally, the broadening of the Mössbauer linewidth (77 K) associated to the shell magnetite sextet from sample BR15 (0.97 mm/s) to sample BR16 (1.01 mm/s) represents an extra support to the model picture of the presence of two nanostructures, more likely Fe_3O_4@ATPS(inner-shell)/NPTS(outer-shell) and Fe_3O_4@

Table 2
Hyperfine parameters obtainded from samples BR15 and BR16. Estimated uncertainties are ± 0.02 mm/s and ± 0.1 T. Error of the spectral areas is estimated at a maximum of 5%.

		Sextet					Doublet			
Sample	*T* (K)	*IS* (mm/s)	*QS* (mm/s	B_{hf} (T)	*Γ* (mm/s)	*A* (%)	*IS* (mm/s)	*QS* (mm/s)	*Γ* (mm/s)	*A* (%)
BR15	297	0.39	−0.13			76	0.41	1.02	0.5	14
	77	0.45	−0.02	50.5	0.56	53	–	–	–	–
		0.40	−0.02	48.2	0.59	28	–	–	–	–
		0.47	0.06	44.5	0.97	19	–	–	–	–
BR16	297	0.37	−0.12	–	–	90	0.46	1.43	0.5	10
	77	0.45	0.00	50.8	0.49	39	–	–	–	–
		0.41	−0.04	48.6	0.64	42	–	–	–	–
		0.41	−0.02	43.7	1.01	19	–	–	–	–

NPTS(inner-shell)/ATPS(outer-shell). Even more visibly, the hyperfine field distributions assessed from the room temperature Mössbauer spectra (see lower panel, right hand-side plots, Figs. 4 and 5) also supports our model picture. Notice that the hyperfine field distribution associated to sample BR15 shows three main features; one lower field distribution correlated to the shell magnetite and two higher field distributions correlated to the core magnetite (site-A and site-B). However, the hyperfine field distribution associated to the BR16 sample shows a clear replica of the three main features as compared to the hyperfine field distribution of sample BR15, being more likely due to the presence of the two above-mentioned nanostructures, namely Fe_3O_4@ATPS(inner-shell)/NPTS (outer-shell) and Fe_3O_4@NPTS(inner-shell)/ATPS(outer-shell). In the BR16 sample we can see one duplicated (replica) lower field distribution assigned to the shell magnetite nanoparticle and two duplicated (replica) higher field distributions assigned to the core magnetite nanoparticle (site-A and site-B). Finally, the 77 K hyperfine field value of the shell magnetite nanoparticle of BR15 sample (44.5 T) is slightly stronger than the hyperfine field value of the shell magnetite nanoparticle of BR16 sample (43.7 T). This is more likely due the influence of the free electron pair of the ATPS's amino group, which increases the interaction between the surface molecular coating and the magnetite shell layer, leading to the enhancement of the exchange interaction within the nanoparticle shell layer. This finding also supports our model picture for the presence and influence of the two nanostructures in the BR16 sample as opposed to one single nanostructure in the BR15 sample. Indeed, while compared to sample BR16 the higher Si/Fe content ratio (0.25) found in sample BR15 indicates the strongest interaction of the Si-based moiety (APTS) with the shell magnetite, likely due to the presence of the amino group.

The magnetic measurements (in the range of ± 70 kOe) were carrying out for both samples (BR15 and BR16) at low (5 K) and high (300 K) temperatures. Magnetization *M* versus magnetic field (*H*) curves recorded at 300 K (see upper panel in Fig. 6) showed no hysteresis, which is consistent with the superparamagnetic behavior of magnetite nanoparticles with average diameter around 10 nm. However, at low temperature (5 K), both samples showed hysteretic *M* vs *H* curves, meaning that both samples are in the blocked state (see lower panel in Fig. 6). At 5 K, coercive fields of 209 Oe and 198 Oe were determining for samples BR15 and BR16, respectively. Moreover, at 5 K the relative remanent magnetization (*Mr*/*Ms*) of 0.16 and 0.15 had been estimating for samples BR15 and BR16, respectively (see Table 3). These findings, namely higher coercive field and higher relative remanent magnetization observed in sample BR15, are in agreement with the picture of the nanoparticle's shell layer built from the analyses of the Mössbauer data, i.e. the enhancement of the exchange interaction within the nanoparticle's shell layer in sample BR15 with respect to sample BR16, which is credited to the stronger interaction of the ATPS's amino group and the nanoparticle's surface. Another interesting feature is the value of the rate *M vs H* in the high field region (above 40 kOe) of the *M* vs *H* curve. In the saturation region, sample BR16 shows a rate of 8×10^{-5} emu/gOe, which is almost twice the one determined for sample BR15. This means that a stronger magnetic disorder sets in the nanoparticle's shell layer in sample BR16, which is

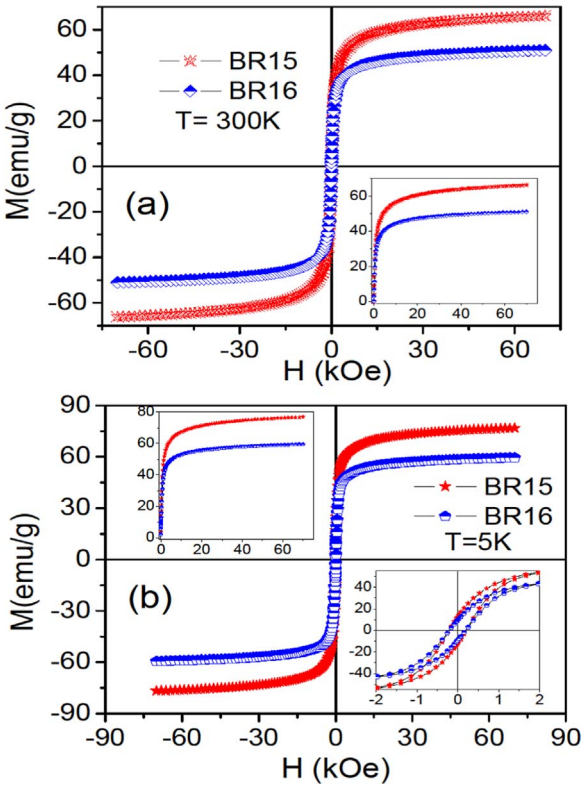

Fig. 6. Magnetization vs magnetic field curves of samples BR15 and BR16 at (a) 300 K and (b) 5 K.

Table 3
Magnetic parameters of samples BR15 and BR16.

Samples	*T* (K)	M_s (emu/g)	M_r (emu/g)	M_r/M_s	H_c (Oe)	d_m (nm)
B15	300	66.0	2.7	0.04	~0	4.08
	5	76.7	12.6	0.16	209	
B16	300	50.9	1.6	0.03	~0	5.42
	5	59.4	9.2	0.15	198	

probably related to the presence of the double molecular coating layer (ATPS plus NPTS), as opposed to the single molecular coating layer (ATPS only) in sample BR15. This finding is in very good agreement with the analysis carried out from the Mössbauer data, as supported by the lower (higher) value of the hyperfine field (linewidth) associated to the sextet assigned to the nanoparticle's shell layer in sample BR16 while compared with the values obtained from sample BR15. The initial magnetization rate of the curves at high temperatures, where the samples are expected to show a superparamagnetic behavior, can be used to estimate the magnetic size of the nanoparticles via the following relation [25]:

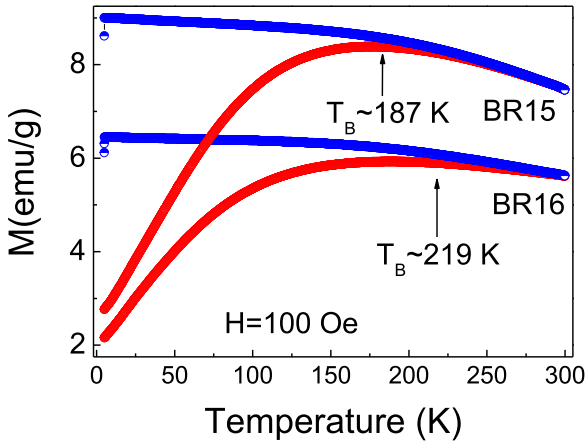

Fig. 7. Zero field-cooled (ZFC) and field-cooled (FC) curves of samples BR15 and BR16.

$$d_m = \left[\frac{18kT\left(\frac{dM}{dH}\right)_{H=0}}{\pi\rho M_S^2}\right]^{\frac{1}{3}},$$

where d_m is the magnetic diameter, k the Boltzmann constant, T the temperature (300 K), dM/dH the slope at near zero-field for samples BR15 (0.0645 emu/gOe) and BR16 (0.0901 emu/gOe), and ρ the density of magnetite (5.18 g/cm^3). The calculation leads to d_m = 4.08 nm and d_m = 5.42 nm for samples BR15 and BR16, respectively. The values we find for the magnetic diameters are smaller than the values calculated from the TEM micrographs. This result strongly suggests the presence of a magnetic disordered shell layer on the nanoparticle's surface as widely reported in the literature [25,26]. Zero field-cooled (ZFC) and field-cooled (FC) curves (see Fig. 7) show features consistent with thermal relaxation of magnetic moments. The ZFC curves show a maximum at 187 K for the sample BR15 and 219 K for the sample BR16. Assuming these values as representatives of the average value of the blocking temperature it means that the particle-particle interaction in the sample BR16 is stronger than the particle-particle interaction taking place in the sample BR15. Once more, the picture of the nanoparticle's shell layer built from the analyses of the Mössbauer data helps to explain the apparent paradox. While in the sample BR15 the amino group of the surface coating (ATPS) faces inward binding to the nanoparticle's surface in the sample BR16 a fraction of the nanoparticles presents the Fe_3O_4@ATPS(inner-shell)/NPTS(outer-shell) structure. In the latter case, more likely the surface molecular layer interface shares the common ethoxy groups (CH_3-O-), leaving outwards the propyl group (CH_3-CH_2-CH_2-), which extends out of the nanoparticle's surface as a tail-like structure. The tail-like structure in the surface of the nanoparticles comprising the sample BR16 may favor inter-particle interaction via van der Walls' attraction more efficiently than the smoother nanoparticle surface (dressed only with ethoxy groups) of the nanoparticles comprising the sample BR16. Indeed, the stronger van der Walls inter-particle attraction among nanoparticles in the sample BR16 favors the magnetic dipole-dipole interaction more efficiently than in the case of nanoparticles in the sample BR15, likely leading to differences in the maximum observed in the ZFC curves, i.e. lower for sample BR15 (187 K) in comparison with sample BR16 (219 K).

4. Conclusions

The synthesis of magnetite nanoparticles via sonoprecipitation was successfully obtained. In addition, surface-functionalization of the as-produced nanosized magnetite via hydrolysis and condensation of alkoxysilane agents (3-aminopropyltrimethoxisilane and propyltrimethoxisilane) was successfully demonstrated. Transmission electron microscopy of the surface-functionalized nanoparticles revealed spherically-shaped magnetite with an average diameter in agreement with the size estimated from x-ray diffraction data. Mössbauer data recorded at 77 K confirmed the magnetite phase at the core of the particle in both samples BR15 and BR16; meanwhile, in the shell region of the core magnetite, the influence of the type of surface molecular coating is more effective than the number of coating layers. Mössbauer data analyses revealed features consistent with unblocked particles and effects related to the free electron pair of the ATPS's amino group, which drives to differences in the hyperfine parameters between the one surface-coating agent (sample BR15) and two surface-coating agents (sample BR16). Magnetization data analysis indicated a strong influence of the surface-coating on the magnetic properties of the as-prepared materials. Once superparamagnetic iron oxide particles with appropriate surface coating are widely used in numerous in vivo applications, as for instance in MRI (magnetic resonance imaging) contrast enhancement, the success of attaching alkoxysilane-coating agents onto SPIO particles is potentially interesting for MRI contrast agent and MPI technologies.

Acknowledgments

The authors acknowledge the financial support of the Brazilian agencies CAPES, CNPq, FAP/DF, and INCT in Nanobiotechnology.

References

[1] S.K. Sahoo, S. Parveen, J.J. Panda, The present and future of nanotechnology in human health care, Nanomed.: Nanotechnol. Biol. Med. 3 (2007) 20–31.
[2] D.T. Nguyen, K. Kim, Controlled magnetic properties of iron oxide-based nanoparticles for smart therapy, KONA Powder Part. J. 33 (2016) 33–47.
[3] V. Tangoulis, M. Skarlis, C.P. Raptopoulou, V. Psycharis, C. Dendrinou-Samara, From molecular magnets to magnetic nanomaterials–deposition of Co_7 single-molecule magnet; theoretical investigation of the exchange interactions, Eur. J. Inorg. Chem. 16 (2014) 2678–2686.
[4] M. Banobre-López, A. Teijeiro, J. Rivas, Magnetic nanoparticle-based hyperthermia for cancer treatment, Rep. Pract. Oncol. Radiother. 18 (2013) 397–400.
[5] C. Sun, J.S.H. Lee, M. Zhang, Magnetic nanoparticles in MR imaging and drug delivery, Adv. Drug Deliv. Rev. 60 (2008) 1252–1265.
[6] M. De Cuyper, M. Hodenius, Z.G.M. Lacava, R.B. Azevedo, M.F. Da Silva, P.C. Morais, M.H.A. Santana, Attachment of water-soluble proteins to the surface of (magnetizable) phospholipid colloids via neutravidin-derivatized phospholipids, J. Colloid Interface Sci. 245 (2002) 274–280.
[7] A.R. Simioni, O.P. Martins, Z.G.M. Lacava, E.C.D. Lima, B.M. Lacava, P.C. Morais, A.C. Tedesco, Cell toxicity studies of albumin-based nanosized magnetic beads, Nanosci. Nanotechnol. 6 (2006) 2413–2415.
[8] P.P. Macaroff, F.L. Primo, R.B. Azevedo, Z.G.M. Lacava, P.C. Morais, A.C. Tedesco, Synthesis and characterization of a magnetic nanoemulsion as a promising candidate for cancer treatment, IEEE Trans. Magn. 42 (2006) 3596–3598.
[9] L. Hao-Li, H. Po-Hong, C. Po-Chun, W. Yau-Yau, C. Jin-Chung, S. Chia-Rui, Y. Tzu-Chen, W. Jiun-Jie, Magnetic resonance imaging enhanced by superparamagnetic iron oxide particles: usefulness for distinguishing between focused ultrasound-induced blood–brain barrier disruption and brain hemorrhage, J. Magn. Res. Imag. 29 (2009) 31–38.
[10] W. Wu, Q. He, C. Jiang, Magnetic iron oxide nanoparticles: synthesis and surface functionalization strategies, Nanoscale Res. Lett. 3 (2008) 397–415.
[11] K. Suzuki, K. Kanisawa, Imaging of quantum confinement and electron wave interference, NTT Tech. Rev. 6 (2008) 1–6.
[12] H. Oka, O. Brovko, M. Corbetta, V. Stepanyuk, D. Sander, J.J. Kirschner, Spin-polarized quantum confinement in nanostructures: scanning tunneling microscopy, Rev. Mod. Phys. 86 (2014) 1127–1167.
[13] L. Zhou, J. Yuan, Y. Wei, Core–shell structural iron oxide hybrid nanoparticles: from controlled synthesis to biomedical applications, J. Mater. Chem. 21 (2013) 2823–2840.
[14] R.F.C. Marques, T.P. Costa, L.C. Varanda, N.J.J. Silva, F.J. Santos, A. Milan, M. Jafelicci Jr, Magnetite nanoparticles tailored with folic acid through modulated surface amine group density, in: VI Encontro SBPMat, Natal-Brazil. Abstracts: SBPMat 2007, p. D579.
[15] J.H. Moon, J.H. Kim, K. Kim, T.H. Kang, B. Kim, C. Kim, J.H. Hahn, J.W. Park, Absolute surface density of the amine group of the aminosilylated thin layers: ultraviolet-visible spectroscopy, second harmonic generation, and synchrotron-radiation photoelectron spectroscopy study, Langmuir 13 (1997) 4305–4310.
[16] A. Campo, T. Sen, J. Lellouche, I.J. Bruce, J. Magn. Magn. Mater. 293 (2005) 33–40.
[17] I.J. Bruce, T. Sen, Surface modification of magnetic nanoparticles with alkoxysilanes and their application in magnetic bioseparations, Langmuir 21 (2005) 7029–7035.
[18] P. Roggwiller, W. Kündig, Mössbauer spectra of superparamagnetic Fe_3O_4, Sol. State Comm. 12 (1973) 901–903.
[19] F.T. Parker, M.W. Foster, D.T. Margulies, A.E. Berkowitz, Spin canting, surface magnetization, and finite-size effects in γ-Fe_2O_3 particles, Phys. Rev. B 47 (1993) 7885–7891.

[20] H.G. Linde, Polyamic acid interactions with aminopropylsilane surface conditioners on metal, J. Appl. Polym. Sci. 40 (1990) 613–622.
[21] I. George, P. Viel, C. Bureau, J. Suski, G. Lécayon, Study of the silicon/ y-APS/ Pyralin assembly interfaces by X-ray photoelectron spectroscopy, Surf. Inter. Anal. 24 (1996) 774–780.
[22] J. Quinton, L. Thomsen, P. Dastoor, Adsorption of organosilanes on iron and aluminium oxide surfaces, Surf. Inter. Anal. 25 (1997) 931–936.
[23] P.W. Atkins, Physical Chemistry, 3ª ed, Oxford University Press, 1987.
[24] S. Yu, G.M. Chow, Synthesis, structural, magnetic, and cytotoxic properties of iron oxide coated iron/iron-carbide nanocomposite particles, J. Appl. Phys. 98 (2005) 114306-1–114306-7.
[25] I. Yaacob, A.C. Nunes, A. Bose, D.O. Shah, Synthesis and characterization of magnetic nanoparticles in spontaneously generated vesicles, J. Colloid Interf. Sci. 168 (1994) 289–301.
[26] E.E. Carpenter, Iron nanoparticles as potential magnetic carriers, J. Magn. Magn. Mater. 225 (2001) 17–20.